

Transport properties of monodisperse and bidisperse hard-sphere colloidal suspensions from multiparticle collision dynamics simulations

Michael P. Howard^{a)}

Department of Chemical Engineering, Auburn University, Auburn, AL 36849, USA

The shear viscosities, long-time self-diffusion coefficients, and sedimentation velocities in monodisperse and bidisperse hard-sphere colloidal suspensions are simulated for volume fractions up to 0.40 using multiparticle collision dynamics with a discrete particle model. The bidisperse suspensions have diameter ratios of 2 and 4 and equal amounts of each particle by volume. All measured properties for monodisperse suspensions are found to be in good agreement with prior literature; however, they highlight the sensitivity of the simulation method to discretization effects. The sedimentation velocities for the bidisperse suspensions are also in reasonable agreement with prior literature, including direction reversal for the smaller particles when the diameter ratio is 4. This work provides reference data for transport properties of colloidal suspensions and establishes the suitability of multiparticle collision dynamics for modeling suspensions of particles with different sizes.

I. INTRODUCTION

Polydispersity is a practical reality of many colloidal suspensions that nontrivially modifies their rheology¹⁻³ and has important implications for industrial processes such as dip coating.⁴ Polydispersity can also be exploited to engineer mesoscale structures, and their resulting properties, in materials.⁵ For example, hard-sphere colloidal particles will spontaneously segregate by size during fast solvent drying,^{6,7} and particle interactions⁸ and dynamics⁹⁻¹³ play a critical in determining the structure that forms. This effect has been used to produce coatings with functional properties such as abrasion-resistance,^{14,15} bacteria-resistance,¹⁶ or controlled release¹⁷ as well supraparticles with engineered porosity.¹⁸

Despite being the simplest case of polydispersity, the transport properties of bidisperse colloidal suspensions are far less well-characterized than those of monodisperse colloidal suspensions. Experimental measurements of the shear viscosity¹⁹ and particle sedimentation coefficients²⁰⁻²³ have been reported for bidisperse suspensions, but the data is sparse and so difficult to interpolate for specific particle sizes and concentrations of interest. Particle-based simulations that faithfully capture solvent-mediated hydrodynamic interactions in the suspension are potentially promising for filling these gaps.^{24,25} However, bidisperse suspensions are more challenging to simulate than monodisperse suspensions because disparity in particle size typically increases the number of particles that must be modeled and the computational costs of the simulations.²⁶ Stokesian dynamics simulations²⁷ have been used to characterize short-time transport properties for bidisperse suspensions,^{28,29} but they are computationally demanding^{30,31} and so can be difficult to use routinely to study long-time or large-scale behaviors.

The purpose of this article is to investigate the suitability of multiparticle collision dynamics^{25,32,33} (MPCD) as a method for simulating bidisperse colloidal suspensions. MPCD uses an explicit, highly simplified solvent that is straightforwardly coupled to colloidal particles,³⁴ and massively parallel open-source software is available to perform MPCD simulations efficiently.^{35,36} I have recently shown that MPCD produces reasonable results for the transport properties of not only monodisperse spherical particles³⁷ but also shape-anisotropic particles such as cubes, octahedra, tetrahedra, and spherocylinders.³⁸ MPCD has also been used to simulate mixtures of spherical and rod-like particles,³⁹ but to my knowledge, it has not yet been applied to bidisperse suspensions of spherical particles. It is important to establish and assess the transport properties of bulk suspensions in MPCD before applying the method to more complex dynamic processes such as self-assembly.

In this article, I use MPCD to simulate the shear viscosity, long-time self-diffusion coefficients, and sedimentation velocities in monodisperse and bidisperse hard-sphere colloidal suspensions as a function of volume fraction. I use particles with three different sizes, giving diameter ratios of 2 and 4 for the bidisperse suspensions. The measured properties are generally in good agreement with theoretical expectations and previous simulations where available, demonstrating the suitability of MPCD for simulating suspensions of particles with different sizes. However, they also highlight the sensitivity of the MPCD method to discretization effects that should be carefully considered.

II. MODEL AND METHODS

In the following, all quantities will be reported in a consistent system of units where m is the unit of mass, ℓ is the unit of length, and ε is the unit of energy. The unit of time is $\tau = \sqrt{m\ell^2/\varepsilon}$ and the unit of temperature is ε/k_B , where k_B is the Boltzmann constant. All simulations were performed using HOOMD-blue^{26,35,40,41} extended

^{a)}Electronic mail: mphoward@auburn.edu

with azplugs.⁴² The versions used for each calculation are noted.

A. Model

The solvent was modeled using MPCD. The solvent particles had mass $1m$, and their number density was $5/\ell^3$. In MPCD, solvent particles do not have pairwise interactions with each other; instead, they evolve in alternating streaming and collision steps. The solvent particles moved according to Newton's equations of motion for 0.1τ , then exchanged momentum with other particles in

$$u(r) = \begin{cases} 4\varepsilon \left[\left(\frac{\sigma}{r - \Delta_{ij}} \right)^{12} - \left(\frac{\sigma}{r - \Delta_{ij}} \right)^6 + \frac{1}{4} \right], & r \leq \Delta_{ij} + 2^{1/6}\sigma, \\ 0, & \text{otherwise} \end{cases}, \quad (1)$$

where r is the distance between the centers of two particles, $\sigma = 1\ell$ sets the length scale for the repulsion, and $\Delta_{ij} = (d_i + d_j)/2 - \sigma$ shifts the divergence of the repulsion based on the diameters of the particles, denoted d_i for particle type i . Three types of particles having diameter 3ℓ , 6ℓ , and 12ℓ were considered (Fig. 1).

The colloidal particles were coupled to the solvent through the collision step using a discrete particle model.³⁴ The surfaces of the colloidal particles were discretized by iteratively subdividing the faces of an icosahedron and rescaling its vertices to lie on the sphere to achieve roughly the same surface density (Fig. 1). These surface sites were connected to their nearest neighbors on the surface and to a central site, used to apply Eq. (1),

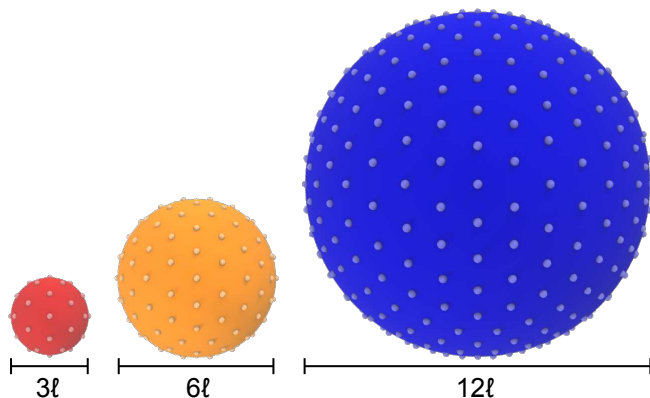


FIG. 1. Particles with diameter 3ℓ , 6ℓ , and 12ℓ along with their discretized surfaces. The number of surface particles for each was 42, 162, and 642, corresponding to surface densities of $1.49\ell^{-2}$, $1.43\ell^{-2}$, and $1.42\ell^{-2}$, respectively. The images were rendered using VMD 1.9.3.⁴⁸

cubic cells with edge length 1ℓ according to the stochastic rotation dynamics rule without angular-momentum conservation.³² The collision angle was 130° , and a rotation axis was randomly chosen for each cell from the unit sphere. A cell-level Maxwell–Boltzmann thermostat^{43,44} was used to maintain constant temperature $1\varepsilon/k_B$, and the grid of collision cells was shifted before each collision along each Cartesian axis by a uniform random amount drawn in the interval between $\pm 0.5\ell$ to ensure Galilean invariance.^{45,46}

The colloidal particles were modeled as nearly hard spheres using the core-shifted Weeks–Chandler–Andersen pairwise interaction potential,⁴⁷

by harmonic springs,

$$u_b(r) = \frac{k}{2}(r - r_0)^2, \quad (2)$$

with a stiff spring constant $k = 5000\varepsilon/\ell^2$ and preferred length r_0 rounded to three decimal places. The surface sites were assigned mass $5m$ and participated in the collisions with the solvent.⁴⁹ The central site was also assigned a mass of $5m$ but did not interact directly with the solvent. Between collisions, all sites comprising a colloidal particle moved according to Newton's equations of motion using conventional molecular dynamics (MD) methods with a Verlet integration scheme (timestep 0.002τ). This approach has been previously shown to reasonably capture the dynamics of single spherical particles,^{34,50} as well as the long-time self-diffusion and sedimentation coefficients of monodisperse spherical³⁷ and shape-anisotropic³⁸ particles.

I considered monodisperse suspensions of all three particle types ($d_1 = 3\ell$, 6ℓ , or 12ℓ) and bidisperse suspensions with $d_1 = 3\ell$ and $d_2 = 6\ell$ or 12ℓ . The simulation box was a cube with edge length $L = 120\ell$ and periodic boundary conditions. A certain number of particles N_i of each type i were dispersed into the box to achieve a desired volume fraction $\phi_i = N_i\pi d_i^3/(6L^3)$ of that type. The particles were placed by randomly selecting sites from a face-centered cubic lattice commensurate with the box and having a lattice constant of roughly $\sqrt{2}d_i$. For the bidisperse suspensions, the larger particles were placed first, then the lattice sites for the smaller particles giving hard-sphere overlap with the larger particles were removed. The total volume fraction $\phi = \sum_i \phi_i$ was varied between 0.01 and 0.40. I considered only equal-volume ($\phi_1 = \phi_2$) bidisperse suspensions because prior Stokesian dynamics simulations²⁸ showed more sensitivity of transport properties to the diameter ratio d_2/d_1

and the total volume fraction ϕ than to the relative composition, ϕ_1/ϕ .

B. Equilibrium structure

The initial configurations were equilibrated for $10^3 \tau$ using isothermal–isochoric MD with a Bussi thermostat⁵¹ (time constant 0.1τ) to maintain constant temperature $1 \varepsilon/k_B$. Hydrodynamic interactions do not affect equilibrium structure, so only the central sites were simulated using a larger timestep of 0.005τ . After equilibration, particle configurations were recorded every 10τ until a certain number were collected (10^3 , 10^4 , and 10^5 for the monodisperse suspensions with $d_1 = 3 \ell$, 6ℓ , and 12ℓ ; 10^4 and 10^5 for the bidisperse suspensions with $d_2/d_1 = 2$ and 4). Five of these configurations, taken at equal time intervals, served as initial configurations for subsequent simulations with hydrodynamic interactions. These simulations were performed using HOOMD-blue version 4.8.2.

The partial static structure factor for particles of types i and j was computed from all recorded configurations using the Ashcroft–Lengreth normalization convention,⁵²

$$S_{ij}(\mathbf{q}) = \frac{1}{\sqrt{N_i N_j}} \left\langle \sum_{n=1}^{N_i} \sum_{p=1}^{N_j} e^{-i\mathbf{q} \cdot (\mathbf{r}_n^{(i)} - \mathbf{r}_p^{(j)})} \right\rangle, \quad (3)$$

where $\mathbf{r}_n^{(i)}$ is the position of a given particle n of type i , \mathbf{q} is a wavevector commensurate with the periodic boundaries of the simulation box, and the angle brackets denote an ensemble average. Under this convention, the total static structure factor is

$$S(\mathbf{q}) = \sum_{i,j} \sqrt{x_i x_j} S_{ij}(\mathbf{q}), \quad (4)$$

where the double sum runs over all particle types i and j , and $x_i = N_i/N$ is the number fraction of type i with $N = \sum_i N_i$ being the total number of particles. The magnitude of the smallest wavevector commensurate with the simulation box was $\Delta q = 2\pi/L$. I calculated the isotropically averaged $S_{ij}(q)$ for wavevector magnitudes $\Delta q \leq q \leq 20\Delta q$ using freud⁵³ (version 3.1.0) with a bin spacing of Δq for wavevector averaging (Figs. S1 and S5).

C. Shear viscosity

I next measured the shear viscosity η of the suspensions using reverse nonequilibrium simulations.^{54,55} The surfaces of the equilibrated particles were discretized, and solvent was added randomly everywhere in the simulation box with velocities randomly thermalized at temperature $1 \varepsilon/k_B$. For only these simulations, the particle configuration was duplicated to make a simulation box that was twice as long in the y direction (i.e., $2L = 240 \ell$). Shear

flow was then generated using an artificial momentum-swapping procedure. Every 0.1τ , solvent particles were sorted into two planar slabs of thickness 1ℓ : a “lower” slab at the bottom of the simulation box and an “upper” slab in the middle of the simulation box in the y direction (spaced apart by L). The particles having the x -component of their velocity closest to a target $0.5 \ell/\tau$ in the lower slab and $-0.5 \ell/\tau$ in the upper slab were identified, and the x -component of the velocity was exchanged between the first 100 pairs of particles sorted in this way. This procedure conserves both linear momentum and kinetic energy for the system, and with appropriate parameters, it produces two regions of opposing steady shear within the same simulation box. The selected parameters are expected to achieve a maximum flow speed of about $0.5 \ell/\tau$ for a pure solvent giving a maximum shear rate less than about $0.01 \tau^{-1}$. Thus, these simulations probe the low-shear regime, as verified in subsequent analysis discussed in Sec. III.

The momentum exchange procedure was carried out for $2 \times 10^4 \tau$ to allow the flow to reach steady state, then a production simulation of $2 \times 10^4 \tau$ was performed to measure the shear viscosity. During the production simulation, the cumulative momentum exchanged by swapping $p_x(t)$ was recorded as a function of time t . The mass-averaged velocity of the suspension in the x direction as a function of position in the y direction, $u_x(y)$, was measured every 10τ using a histogram of the solvent and all sites that comprised the particles in y with bin width 0.5ℓ (Figs. S3 and S7). The average rate of momentum transfer \dot{p}_x was computed over the entire production simulation. The shear rate $\dot{\gamma} = dv_x/dy$ was extracted by a linear fit of the measured velocity, excluding a region of thickness 24ℓ centered around each momentum-exchange slab and applying the symmetry of the opposing shear flows. The shear viscosity η was then computed as

$$\eta = \frac{1}{2L^2} \frac{\dot{p}_x}{\dot{\gamma}}. \quad (5)$$

I repeated this procedure for the first three equilibrated configurations, and I report the mean η with uncertainty estimated as one standard error of the mean from these simulations. The simulations were performed using HOOMD-blue 5.3.1 with azplugins 1.1.0.

D. Long-time self-diffusion coefficient

The long-time self-diffusion coefficient D_i for particles of type i was determined from equilibrium simulations. Discretized, solvated initial particle configurations were prepared and equilibrated for $10^3 \tau$, then a production simulation of $5 \times 10^4 \tau$ was performed during which the particle positions were recorded every 10τ . The average mean squared displacement $\langle \Delta r_i^2(t) \rangle$ of a particle of type i after time t was computed up to $2 \times 10^4 \tau$ using all configurations as independent time origins and averaging over all particles. The long-time self-diffusion coefficient

was then computed as

$$D_i = \frac{1}{6} \lim_{t \rightarrow \infty} \frac{d\langle \Delta r_i^2 \rangle}{dt}. \quad (6)$$

The time derivative of $\langle \Delta r_i^2 \rangle$ was evaluated numerically (Figs. S4 and S8), and the long-time limit was taken by averaging its value for $t \geq 10^4 \tau$.

Self-diffusion coefficients simulated in cubic boxes with periodic boundary conditions are known to be reduced compared to their values in an infinitely large box. This finite-size effect can be corrected by adding^{56,57}

$$\Delta D = \xi \frac{k_B T}{6\pi\eta L} \quad (7)$$

to the simulated value, where $\xi = 2.837297$ is a constant related to summing long-ranged hydrodynamic interactions over a cubic lattice of simulation boxes.⁵⁸ The mean value and uncertainty (one standard error of the mean) of the self-diffusion coefficients were determined from five independent simulations, then corrected using Eq. (7) with uncertainty propagation. The simulations were performed using HOOMD-blue 5.0.1.

E. Sedimentation velocity

The sedimentation velocity U_i for particles of type i was determined from force-driven nonequilibrium simulations. The same solvated initial configurations were used as for the self-diffusion coefficients, but now a body force f_i was applied to particles of type i in the positive x direction to simulate sedimentation. I used a force of $0.5 \varepsilon/\ell$ for the particles with diameter 6ℓ , and I made $f_i \sim d_i^3$ to be consistent with sedimentation resulting from a density mismatch. The body force was distributed equally between the central and surface sites. A counterforce was also applied to all solvent particles to ensure the suspension was force free. Sedimentation was simulated for $10^3 \tau$ to reach steady state. The sedimentation velocity U_i averaged over all particles of type i was then recorded every 0.102τ during a $5 \times 10^4 \tau$ production simulation and averaged over all measurements. The reason for this sampling rate is to collect samples at different offsets relative to the collision period.

Similarly to diffusion coefficients, sedimentation velocities simulated in cubic boxes with periodic boundary conditions are also reduced compared to their values in an infinitely large box. For monodisperse suspensions, the correction added to the simulated value is⁵⁹

$$\Delta U_1 = \frac{\xi}{6\pi\eta L} S(0) f_1, \quad (8)$$

where $S(0) = \lim_{q \rightarrow 0} S(q)$ is the limit of the static structure factor approaching the zero wavevector. This value was extracted from the equilibrium simulation data by fitting to a quadratic form $c_1 + c_2 q^2$ for $0.15 \ell^{-1} \leq q \leq$

$0.5 \ell^{-1}$ for diameters 3ℓ and 6ℓ and $q \leq 0.3 \ell^{-1}$ for diameter 12ℓ (Fig. S1) and extrapolating to $q = 0$. For bidisperse suspensions, the corrections for each particle type are more complicated and involve the partial static structure factors²⁸

$$\Delta U_1 = \frac{\xi}{6\pi\eta L} \left[S_{11}(0) f_1 + \sqrt{\frac{x_2}{x_1}} S_{12}(0) f_2 \right] \quad (9)$$

$$\Delta U_2 = \frac{\xi}{6\pi\eta L} \left[\sqrt{\frac{x_1}{x_2}} S_{12}(0) f_1 + S_{22}(0) f_2 \right], \quad (10)$$

where $S_{ij}(0) = \lim_{q \rightarrow 0} S_{ij}(q)$. These values were fit and extrapolated in the same way as for the monodisperse suspensions using the fitting range for q associated with the larger particle (Fig. S5). As for the self-diffusion coefficients, the mean value and uncertainty (one standard error of the mean) of the sedimentation velocities were determined from five independent simulations, then corrected using Eqs. (8)–(10) with uncertainty propagation. The simulations were performed using HOOMD-blue 5.0.1 with azplugins 1.1.0.

III. RESULTS AND DISCUSSION

A. Monodisperse suspensions

I started by characterizing the transport properties of the monodisperse suspensions. It is expected that transport properties for monodisperse suspensions of particles with different diameters should collapse as a function of the volume fraction ϕ when made nondimensional by their values in the dilute limit. I and others have previously simulated the self-diffusion and sedimentation of monodisperse hard-sphere colloidal suspensions using MPCD,^{37,38,50} typically finding reasonable agreement with theory, experiments, and other simulation methods. However, it is also known that MPCD simulations can be sensitive to the size of the particles⁶⁰ as well as to their surface discretization,^{34,50} so it was important to establish whether theoretical consistency was obtained for the monodisperse suspensions before simulating their bidisperse mixtures.

I first considered the shear viscosity η of the monodisperse suspensions (Fig. 2). The simulations should probe the low-shear limit, for which an approximation of the viscosity has been derived,⁶¹

$$\frac{\eta}{\eta_0} = g^+ \left[1 + \frac{1.44(\phi g^+)^2}{1 - 0.1241\phi + 10.46\phi^2} \right]. \quad (11)$$

In this approximation, η_0 is the viscosity of the pure solvent, and g^+ is the value of the hard-sphere radial distribution function at contact. I measured an MPCD solvent viscosity of $\eta_0 = 3.95 \varepsilon\tau/\ell^3$ using the same reverse nonequilibrium simulation protocol as for the suspensions, which is in excellent agreement with the theoretical expectation^{62–64} and previously reported measurements,⁶⁵ while g^+ was modeled using the

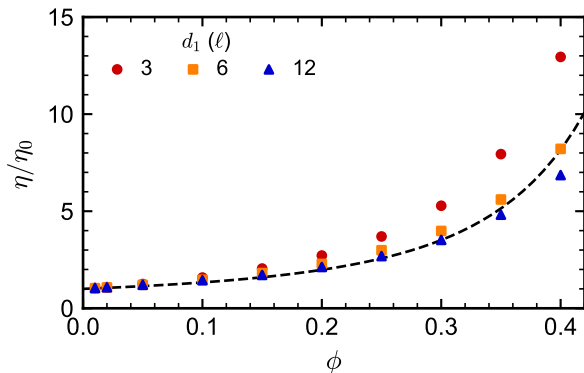


FIG. 2. Simulated shear viscosity η as a function of volume fraction ϕ for monodisperse suspensions of particles with diameter d_1 . The dashed line is Eq. (11).

Carnahan–Starling equation of state,⁶⁶

$$g^+ = \frac{1 - \phi/2}{(1 - \phi)^3}. \quad (12)$$

The simulated shear viscosity for the monodisperse suspensions was in generally good agreement with Eq. (11). The viscosity for diameter 3ℓ was consistently somewhat larger than expected, which is most obvious for the larger volume fractions. The viscosity for diameters 6ℓ and 12ℓ were in line with expectations, although the viscosity for diameter 12ℓ was consistently smaller than for diameter 6ℓ . For self-consistency, the measured suspension viscosities were used for calculating finite-size corrections to the self-diffusion and sedimentation coefficients.

I next analyzed the long-time self-diffusion coefficient D_1 of the monodisperse suspensions (Fig. 3), which is theoretically expected to be⁶⁷

$$\frac{D_1}{D_{0,1}} = \frac{1 - 9\phi/32}{1 + H + (\phi/\phi_0)/(1 - \phi/\phi_0)^2}, \quad (13)$$

where $D_{0,1}$ is the long-time self-diffusion coefficient of a single particle,

$$H = \frac{2b^2}{1-b} - \frac{c}{1+2c} - \frac{bc(2+c)}{(1+c)(1-b+c)} \quad (14)$$

with $b = \sqrt{9\phi/8}$ and $c = 11\phi/16$, and $\phi_0 = (4/3)^3/(7\ln 3 - 8\ln 2 + 2) \approx 0.5718$. This theoretical expectation is in reasonable agreement with experimental data⁶⁷ as well as Stokesian dynamics simulations available for a limited set of larger volume fractions⁶⁸ [Fig. 3(b)].

To compare the MPCD simulations with Eq. (13), I performed 100 additional simulations of a single particle to measure $D_{0,1}$ (Fig. S10 and Table I). The simulated values of $D_{0,1}$ were consistently smaller than the theoretical expectation for a sphere with no-slip boundary conditions, $D_{0,1} = k_B T / (3\pi\eta_0 d_1)$, with errors of 15.3%, 0.7%, and 4.0% for diameters 3ℓ , 6ℓ , and 12ℓ , respectively.

TABLE I. Long-time self-diffusion coefficient $D_{0,1}$ and sedimentation velocity $U_{0,1}$ for a single particle with different diameter d_1 . The applied force f_1 in the sedimentation simulations was proportional to the particle volume with $f_1 = 0.5\varepsilon/\ell$ for $d_1 = 6\ell$. The simulated values are compared to theoretical expectations for a sphere with no-slip boundary conditions.

d_1 (ℓ)	$D_{0,1}$ ($10^{-3}\ell^2/\tau$)		$U_{0,1}$ ($10^{-3}\ell/\tau$)	
	expected	simulated	expected	simulated
3	8.94	7.57 ± 0.23	0.56	0.48 ± 0.03
6	4.47	4.44 ± 0.16	2.24	2.09 ± 0.03
12	2.24	2.15 ± 0.07	8.94	8.67 ± 0.03

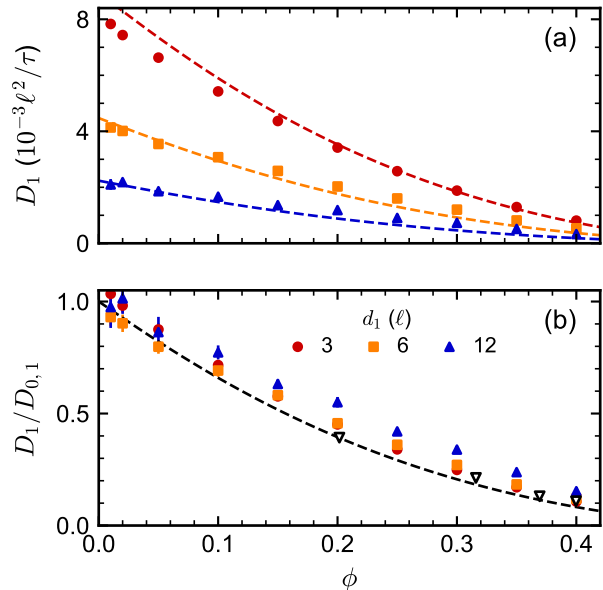


FIG. 3. (a) Simulated long-time self-diffusion coefficient D_1 as a function of volume fraction ϕ for monodisperse suspensions of particles with diameter d_1 . The dashed line is Eq. (13) with $D_{0,1}$ set to its theoretically expected value. (b) The same as (a) but the simulated D_1 is normalized by the simulated single-particle self-diffusion coefficient $D_{0,1}$. The open symbols are the Stokesian dynamics results of Ref. 68.

The simulated suspension long-time self-diffusion coefficients D_1 were somewhat smaller than expected from Eq. (13) at small volume fractions but then tended to be somewhat larger at large volume fractions [Fig. 3(a)]. This weaker volume-fraction dependence is clearer when the simulated D_1 is normalized by the simulated $D_{0,1}$ [Fig. 3(b)]: all three diameters gave $D_1/D_{0,1}$ similar to each other, and all had a somewhat weaker dependence on ϕ than expected from Eq. (13).

In previous work,^{37,38} I did not measure the suspension shear viscosity so I assumed that the shear viscosity and long-time self-diffusion coefficient satisfied the generalized Stokes–Einstein relationship,⁶⁹ $\eta/\eta_0 = D_{0,1}/D_1$, to apply finite-size corrections. Since D_1 and η have both been measured here, I tested the validity of this assump-

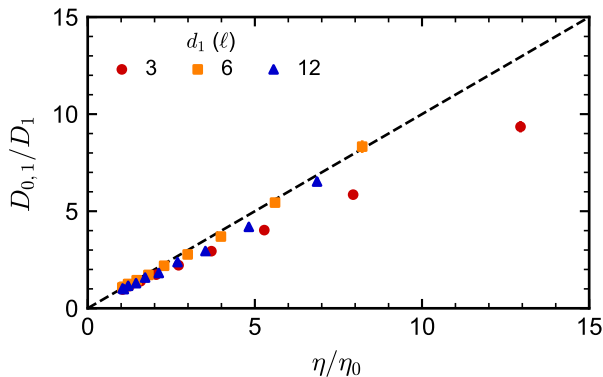


FIG. 4. Test of the generalized Stokes–Einstein relationship between the simulated shear viscosity η and long-time self-diffusion coefficient D_1 for monodisperse suspensions of particles with diameter d_1 using the data from Figs. 2 and 3. The dashed line, $D_{0,1}/D_1 = \eta/\eta_0$, is the theoretical expectation.

tion by comparing the proportionality of the two quantities (Fig. 4). I found that the generalized Stokes–Einstein relationship is well-satisfied for diameters 6ℓ and 12ℓ , but there was some discrepancy for diameter 3ℓ . The previous work used particles with diameter 6ℓ , so the Stokes–Einstein assumption seems to be justified in that case.

I last measured the sedimentation velocity U_1 of the monodisperse suspensions under the applied force described in Sec. II E. The static structure factor at zero wavevector, $S(0)$, was needed to apply finite-size corrections to U_1 , so I extrapolated it from the measured $S(q)$ (Fig. S1). I confirmed that, as expected, the simulated values of $S(0)$ were the same for all three particle diameters (Fig. S2). The values of $S(0)$ also matched the theoretical expectation based on the isothermal compressibility of the Carnahan–Starling equation of state.⁶⁶ This agreement justifies the use of the Carnahan–Starling equation of state to also compute g^+ in Eq. (11). The simulated values of $S(0)$ were used to apply the finite-size corrections to U_1 .

I then compared the sedimentation velocities with a semi-empirical approximation for U_1 ,²⁸

$$\frac{U_1}{U_{0,1}} = (1 - \phi)^{6.5464}, \quad (15)$$

where $U_{0,1}$ is the sedimentation velocity of a single particle. Note that the first-order series expansion of Eq. (15) matches Batchelor’s well-known result for the dilute limit⁷⁰ within rounding to two digits. It is also in good agreement with Stokesian dynamics simulations for modest volume fractions,²⁸ with those simulations giving somewhat larger values of U_1 at larger volume fractions (Fig. 5).

To compare the MPCD simulations with Eq. (15), I performed sedimentation simulations of a single particle (800 simulations for diameter 3ℓ , 100 simulations for diameters 6ℓ and 12ℓ) to measure $U_{0,1}$ (Table I). As for the

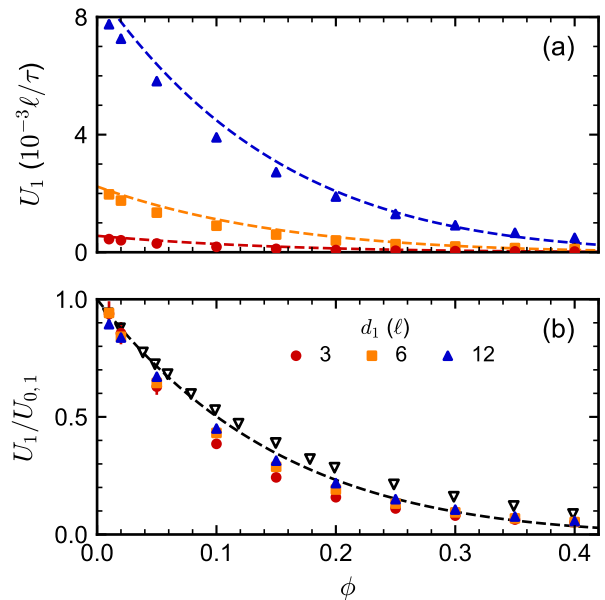


FIG. 5. (a) Simulated sedimentation velocity U_1 as a function of volume fraction ϕ for monodisperse suspensions of particles with diameter d_1 . The dashed line is Eq. (15) with $U_{0,1}$ set to its theoretically expected value. The applied force f_1 was proportional to the particle volume with $f_1 = 0.5 \varepsilon/\ell$ for $d_1 = 6\ell$. (b) The same as (a) but the simulated U_1 is normalized by the simulated single-particle sedimentation velocity $U_{0,1}$. The open symbols are the Stokesian dynamics results of Ref. 28.

self-diffusion coefficient, the simulated values of $U_{0,1}$ were typically smaller than theoretically expected for a sphere with no-slip boundary conditions, $U_{0,1} = f_1/(3\pi\eta_0 d_1)$, with errors of 14.3%, 6.7%, 3.0% for diameters 3ℓ , 6ℓ , and 12ℓ , respectively. The simulated U_1 for the suspensions were then also smaller than expected based on Eq. (15) [Fig. 5(a)] for most volume fractions, with some crossover at the largest volume fractions. Interestingly, after normalizing by the simulated $U_{0,1}$, the simulated U_1 had a somewhat stronger volume fraction dependence than expected [Fig. 5(b)] at smaller volume fractions, although the self-diffusion coefficient had a weaker dependence. This dependence became weaker than expected for larger volume fractions.

Overall, particles with diameter 3ℓ exhibited the largest deviations from theoretical expectations for the suspension viscosity η as well as the long-time self-diffusion coefficient $D_{0,1}$ and sedimentation velocity $U_{0,1}$ of a single particle, but $D_1/D_{0,1}$ and $U_1/U_{0,1}$ still had a similar volume-fraction dependence as the other particles. The particles with diameter 3ℓ also had the largest departure from the generalized Stokes–Einstein relationship between D_1 and η . These errors for diameter 3ℓ might be related to known artifacts in MPCD when the ratio of the diameter of a colloidal particle to the edge length of the collision cell becomes small,⁶⁰ as the edge length of the collision cell is roughly the length scale over which hydrodynamics can be resolved.⁷¹ Particles with

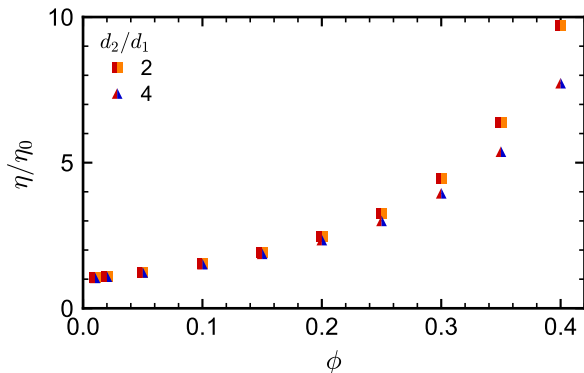


FIG. 6. Simulated shear viscosity η as a function of volume fraction ϕ for bidisperse suspensions of particles with diameters $d_1 = 3\ell$ and varied d_2 . The suspensions had equal amounts of each particle by volume.

diameters 6ℓ and 12ℓ gave results that were more closely aligned with theoretical expectations, but there were still some differences between the two particle sizes. These differences might then be related to small differences in their discrete representations. Together, these discrepancies highlight the potential sensitivity of the MPCD method to discretization effects, which should be carefully considered. However, the results for all particle sizes seemed to be reasonably consistent with each other, particularly after normalizing by values for a single particle, and with theoretical expectations so I proceeded to simulate bidisperse suspensions.

B. Bidisperse suspensions

Following the same workflow as for the monodisperse suspensions, I first measured the viscosity η of the bidisperse suspensions in the low-shear limit (Fig. 6). The viscosity had a similar dependence on volume fraction for both diameter ratio 2 and 4, with η for diameter ratio 2 increasing somewhat faster with ϕ . This behavior is qualitatively consistent with models for the shear viscosity of polydisperse suspensions based on effective volume fraction^{1,72,73} because the maximum attainable suspension volume fraction, at which the shear viscosity diverges in these models, increases with diameter ratio.⁷⁴ However, I note that the simulated shear viscosity was larger than predicted by these models for the larger volume fractions. Further, η for the monodisperse suspension with diameter 6ℓ was larger than for diameter 12ℓ , although both should be the same. I attributed these differences to discretization artifacts in Sec. III A, and they may contribute here to differences in the ϕ -dependence of the bidisperse suspension shear viscosity.

I next characterized the long-time self-diffusion coefficients D_1 and D_2 for both particle sizes in the bidisperse suspensions. Regardless of the size of the larger particle d_2 , D_1 had nearly the same value for the particles

with $d_1 = 3\ell$ [Fig. 7(a)–(b)]. As expected, D_2 was about twice as large for $d_2 = 6\ell$ than for $d_2 = 12\ell$ [Fig. 7(c)]; however, $D_2/D_{0,2}$ was nearly the same for both diameter ratios [Fig. 7(d)]. This collapse is qualitatively consistent with the particles following a generalized Stokes–Einstein relationship with a similar suspension viscosity. I plotted $D_{0,i}/D_i$ against η for the bidisperse suspensions (Fig. S9), and I confirmed that the two were roughly linearly proportional for both types of particles. However, as for the monodisperse suspensions, the larger particles had the proportionality expected from the generalized Stokes–Einstein relationship, but the smaller particles had a smaller proportionality constant than expected.

I last considered the sedimentation velocities U_1 and U_2 for both particle sizes in the bidisperse suspensions. I extrapolated the partial static structure factors at zero wavevector $S_{ij}(0)$ from the simulated $S_{ij}(q)$ (Figs. S5 and S6) and used these values to apply finite-size corrections. An approximation of the sedimentation velocity in polydisperse suspensions has been developed,⁷⁵

$$\frac{U_1}{U_{0,1}} = (1 - \phi)^{c_{11}} [1 + (c_{11} - c_{12})\phi/2] \quad (16)$$

$$\frac{U_2}{U_{0,2}} = (1 - \phi)^{c_{22}} [1 + (c_{22} - c_{21})\phi/2] \quad (17)$$

with $c_{11} = c_{22} = 6.5464$, while $c_{12} = \{11.966, 29.392\}$ and $c_{21} = \{4.7167, 4.0146\}$ for $d_2/d_1 = \{2, 4\}$.²⁸ This approximation is in reasonable agreement with Stokesian dynamics simulation results²⁸ [Fig 8(b) and (d)].

As for the monodisperse suspensions, the sedimentation velocities U_1 and U_2 simulated using MPCD were consistently somewhat smaller than theoretically expected [Fig. 7(a) and (c)]. The sedimentation velocity for the larger particles with diameters 6ℓ or 12ℓ was typically in somewhat better agreement than for the smaller particles with diameter 3ℓ ; this result is sensible given the issues noted for the smallest particles in the monodisperse suspensions. However, good agreement with both theoretical expectations and Stokesian dynamics simulations was found after normalization by the simulated values for a single particle [Figs. 8(b) and (d)].

It is particularly noteworthy that the MPCD simulations correctly capture the reversal in direction of U_1 for diameter ratio 4, even achieving a fastest speed at a similar volume fraction as expected from Eq. (16). Qualitatively, this reversal is driven by solvent backflow induced by the sedimentation of the larger particles, so the MPCD simulations are reasonably capturing this hydrodynamic behavior. There are some quantitative differences that, based on the monodisperse suspensions, might be resolved by using larger particles through proportional increases in both d_1 and d_2 . Unfortunately, I was not able to test this at present due to computational cost.

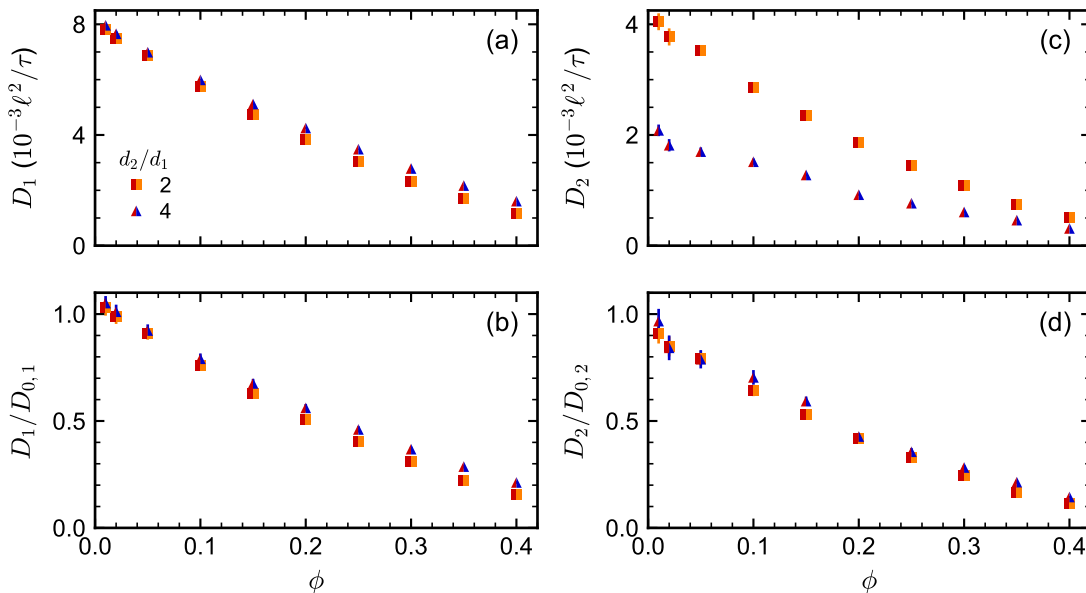


FIG. 7. Simulated long-time self-diffusion coefficients (a) D_1 and (c) D_2 as a function of volume fraction ϕ for bidisperse suspensions of particles with diameter $d_1 = 3\ell$ and varied d_2 . The suspensions had equal amounts of each particle by volume. (b) and (d) are the same as (a) and (c) but D_1 and D_2 are normalized by the simulated single-particle self-diffusion coefficients $D_{0,1}$ and $D_{0,2}$.

IV. CONCLUSIONS

Using MPCD with a discrete particle model, I have simulated the shear viscosity, long-time self-diffusion coefficient, and sedimentation velocity in monodisperse and bidisperse hard-sphere colloidal suspensions as a function of volume fraction for three different sizes of particles. The results for the monodisperse suspensions were compared to theoretical expectations and prior simulations, generally finding reasonable agreement. Discrepancies between results for the different particle sizes highlight the potential for discretization artifacts in MPCD from both the size of the particle relative to the collision cell and the representation of the particle surface. The sedimentation velocities for the bidisperse suspensions were also in reasonable agreement with theoretical expectations and prior simulations.

These simulations provide useful reference data on the transport properties of colloidal suspensions that supplements existing literature. This work also establishes the suitability of the MPCD method for simulating suspensions containing multiple types of particles. MPCD is a convenient method for simulating hydrodynamic interactions near solid boundaries as well as a variety of soft materials, not only particles, because of its simple particle-based solvent. This work lays the groundwork for using MPCD to simulate more complex dynamic processes for colloidal suspensions. For example, MPCD might be used to simulate the drying-induced assembly of size-stratified particle coatings, as well as for measuring transport coefficients that can be used to model this

process at a continuum level.

SUPPLEMENTARY MATERIAL

See the supplementary material for measured and extrapolated static structure factors, velocities in reverse nonequilibrium simulations, and time derivatives of mean squared displacements for all suspensions at representative volume fractions.

CONFLICTS OF INTEREST

The author has no conflicts to disclose.

DATA AVAILABILITY

The data that support the findings of this study are available from the author upon reasonable request.

ACKNOWLEDGMENTS

This material is based upon work supported by the National Science Foundation under Award No. 2310724 and the International Fine Particle Research Institute. This work used Delta at the National Center for Supercomputing Applications through allocation CHM250006 from the Advanced Cyberinfrastructure Coordination

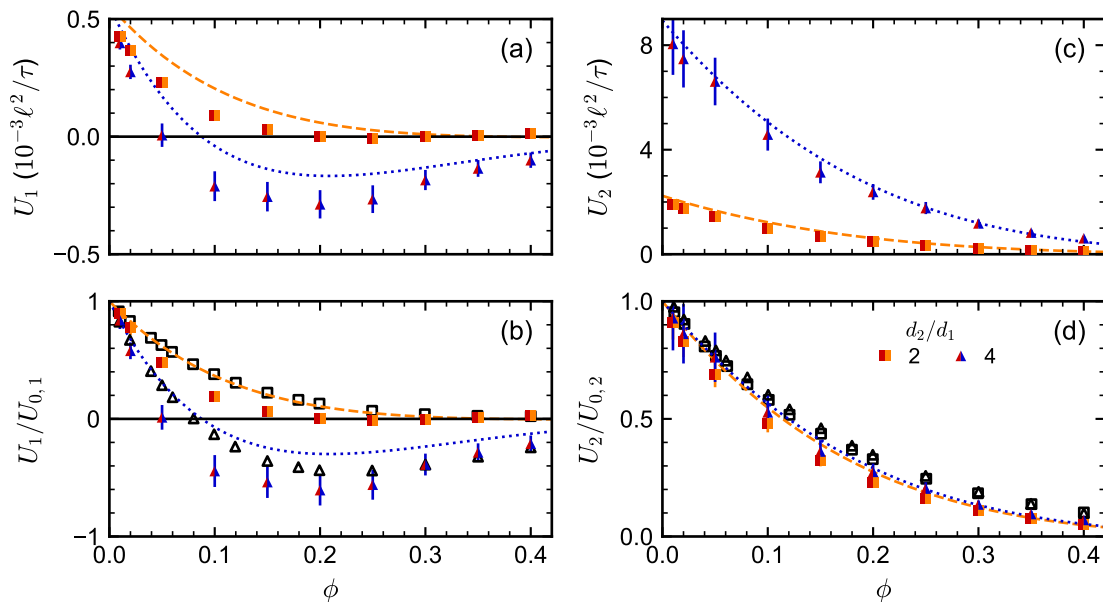


FIG. 8. Simulated sedimentation velocities (a) U_1 and (c) U_2 as a function of volume fraction ϕ for bidisperse suspensions of particles with diameter $d_1 = 3\ell$ and varied d_2 . The suspensions had equal amounts of each particle by volume, and the applied force f_1 was proportional to the particle volume with $f_1 = 0.5 \varepsilon/\ell$ for $d_1 = 6\ell$. (b) and (d) are the same as (a) and (c) but U_1 and U_2 are normalized by the simulated single-particle sedimentation velocities $U_{0,1}$ and $U_{0,2}$. The dashed and dotted lines are Eqs. (16) and (17) for $d_2/d_1 = 2$ and 4, respectively, using the theoretically expected values of $U_{0,1}$ and $U_{0,2}$. The open symbols are the Stokesian dynamics results of Ref. 28.

Ecosystem: Services & Support (ACCESS) program,⁷⁶ which is supported by National Science Foundation grants #2138259, #2138286, #2138307, #2137603, and #2138296. This work was also completed with resources provided by the Auburn University Easley Cluster.

¹P. F. Luckham and M. A. Ukeje, “Effect of particle size distribution on the rheology of dispersed systems,” *Journal of Colloid and Interface Science* **220**, 347–356 (1999).

²S. R. Rastogi, N. J. Wagner, and S. R. Lustig, “Microstructure and rheology of polydisperse, charged suspensions,” *Journal of Chemical Physics* **104**, 9249–9258 (1996).

³S. Pednekar, J. Chun, and J. F. Morris, “Bidisperse and polydisperse suspension rheology at large solid fraction,” *Journal of Rheology* **62**, 513–526 (2018).

⁴D.-H. Jeong, M. K. H. Lee, V. Thiévenaz, M. Z. Bazant, and A. Sauret, “Dip coating of bidisperse particulate suspensions,” *Journal of Fluid Mechanics* **936**, A36 (2022).

⁵S. Fernando, M. K. Gunawardana, T. Thilanka, and S. R. Bhatia, “Evaporation-induced stratification in nanoparticle coatings: A panoramic overview of single-step processes to manufacture multifunctional films,” *Industrial & Engineering Chemistry Research* **64**, 18002–18012 (2025).

⁶A. Fortini, I. Martín-Fabiani, J. L. De La Haye, P.-Y. Dugas, M. Lansalot, F. D’Agosto, E. Bourgeat-Lami, J. L. Keddie, and R. P. Sear, “Dynamic stratification in drying films of colloidal mixtures,” *Physical Review Letters* **116**, 118301 (2016).

⁷M. P. Howard, A. Nikoubashman, and A. Z. Panagiotopoulos, “Stratification dynamics in drying colloidal mixtures,” *Langmuir* **33**, 3685–3693 (2017).

⁸J. Zhou, Y. Jiang, and M. Doi, “Cross interaction drives stratification in drying film of binary colloidal mixtures,” *Physical Review Letters* **118**, 108002 (2017).

⁹R. P. Sear and P. B. Warren, “Diffusiophoresis in nonadsorbing polymer solutions: The asakura-oosawa model and stratification in drying films,” *Physical Review E* **96**, 062602 (2017).

¹⁰A. Statt, M. P. Howard, and A. Z. Panagiotopoulos, “Influence of hydrodynamic interactions on stratification in drying mixtures,” *Journal of Chemical Physics* **149**, 024902 (2018).

¹¹M. P. Howard and A. Nikoubashman, “Stratification of polymer mixtures in drying droplets: Hydrodynamics and diffusion,” *Journal of Chemical Physics* **153**, 054901 (2020).

¹²W. Liu, J. Midya, M. Kappl, H.-J. Butt, and A. Nikoubashman, “Segregation in drying binary colloidal droplets,” *ACS Nano* **13**, 4972–4979 (2019).

¹³J. S. Park, J. Yun, B. Chun, and H. W. Jung, “Mild stratification in drying films of colloidal mixtures,” *Soft Matter* **18**, 3487–3497 (2022).

¹⁴J. D. Tinkler, A. Scacchi, H. R. Kothari, H. Tulliver, M. Argaiz, A. J. Archer, and I. Martín-Fabiani, “Evaporation-driven self-assembly of binary and ternary colloidal polymer nanocomposites for abrasion resistant applications,” *Journal of Colloid and Interface Science* **581**, 729–740 (2021).

¹⁵N. Kargarfard, F. Simon, K. Schlenstedt, L. Ulschberger, B. Voit, M. Gedan-Smolka, and C. Zimmerer, “Self-stratifying powder coatings based on eco-friendly, solvent-free epoxy/silicone technology for simultaneous corrosion and weather protection,” *Progress in Organic Coatings* **161**, 106443 (2021).

¹⁶Y. Dong, M. Argaiz, B. He, R. Tomovska, T. Sun, and I. Martín-Fabiani, “Zinc oxide superstructures in colloidal polymer nanocomposite films: Enhanced antibacterial activity through slow drying,” *ACS Applied Polymer Materials* **2**, 626–635 (2020).

¹⁷H. Le, T. J. Murdoch, A. Barquero, R. Tomovska, and I. Martín-Fabiani, “Harnessing particle size segregation to tune molecular additive distribution in coatings,” *Industrial & Engineering Chemistry Research* **65**, 1241–1251 (2026).

¹⁸W. Liu, M. Kappl, and H.-J. Butt, “Tuning the porosity of supraparticles,” *ACS Nano* **13**, 13949–13956 (2019).

- ¹⁹B. E. Rodriguez, E. W. Kaler, and M. S. Wolfe, “Binary mixtures of monodisperse latex dispersions. 2. viscosity,” *Langmuir* **8**, 2382–2389 (1992).
- ²⁰S. Mirza and J. Richardson, “Sedimentation of suspensions of particles of two or more sizes,” *Chemical Engineering Science* **34**, 447–454 (1979).
- ²¹M. Al-Naafa and M. S. Selim, “Sedimentation of polydisperse concentrated suspensions,” *Canadian Journal of Chemical Engineering* **67**, 253–264 (1989).
- ²²M. A. Al-Naafa and M. S. Selim, “Sedimentation of monodisperse and bidisperse hard-sphere colloidal suspensions,” *AIChE Journal* **38**, 1618–1630 (1992).
- ²³R. H. Davis and K. H. Birdsell, “Hindered settling of semidilute monodisperse and polydisperse suspensions,” *AIChE Journal* **34**, 123–129 (1988).
- ²⁴D. S. Bolintineanu, G. S. Grest, J. B. Lechman, F. Pierce, S. J. Plimpton, and P. R. Schunk, “Particle dynamics modeling methods for colloid suspensions,” *Computational Particle Mechanics* **1**, 321–356 (2014).
- ²⁵M. P. Howard, A. Nikoubashman, and J. C. Palmer, “Modeling hydrodynamic interactions in soft materials with multiparticle collision dynamics,” *Current Opinion in Chemical Engineering* **23**, 34–43 (2019).
- ²⁶M. P. Howard, J. A. Anderson, A. Nikoubashman, S. C. Glotzer, and A. Z. Panagiotopoulos, “Efficient neighbor list calculation for molecular simulation of colloidal systems using graphics processing units,” *Computer Physics Communications* **203**, 45–52 (2016).
- ²⁷J. F. Brady, R. J. Phillips, J. C. Lester, and G. Bossis, “Dynamic simulation of hydrodynamically interacting suspensions,” *Journal of Fluid Mechanics* **195**, 257–280 (1988).
- ²⁸M. Wang and J. F. Brady, “Short-time transport properties of bidisperse suspensions and porous media: A stokesian dynamics study,” *Journal of Chemical Physics* **142**, 094901 (2015).
- ²⁹M. Wang, M. Heinen, and J. F. Brady, “Short-time diffusion in concentrated bidisperse hard-sphere suspensions,” *Journal of Chemical Physics* **142**, 064905 (2015).
- ³⁰M. Wang and J. F. Brady, “Spectral ewald acceleration of stokesian dynamics for polydisperse suspensions,” *Journal of Computational Physics* **306**, 443–477 (2016).
- ³¹A. M. Fiore and J. W. Swan, “Fast stokesian dynamics,” *Journal of Fluid Mechanics* **878**, 544–597 (2019).
- ³²A. Malevanets and R. Kapral, “Mesoscopic model for solvent dynamics,” *Journal of Chemical Physics* **110**, 8605–8613 (1999).
- ³³G. Gompper, T. Ihle, D. M. Kroll, and R. G. Winkler, “Multiparticle collision dynamics: A particle-based mesoscale simulation approach to the hydrodynamics of complex fluids,” in *Advanced Computer Simulation Approaches for Soft Matter Sciences III*, edited by C. Holm and K. Kremer (Springer Berlin Heidelberg, Berlin, Heidelberg, 2009) pp. 1–87.
- ³⁴S. Poblete, A. Wysocki, G. Gompper, and R. G. Winkler, “Hydrodynamics of discrete-particle models of spherical colloids: A multiparticle collision dynamics simulation study,” *Physical Review E* **90**, 033314 (2014).
- ³⁵M. P. Howard, A. Z. Panagiotopoulos, and A. Nikoubashman, “Efficient mesoscale hydrodynamics: Multiparticle collision dynamics with massively parallel gpu acceleration,” *Computer Physics Communications* **230**, 10–20 (2018).
- ³⁶E. Westphal, S. Goh, R. G. Winkler, and G. Gompper, “Htmppc: A heavily templated c++ library for large scale particle-based mesoscale hydrodynamics simulations using multiparticle collision dynamics,” *Computer Physics Communications* **309**, 109494 (2025).
- ³⁷Y. M. Wani, P. G. Kovakas, A. Nikoubashman, and M. P. Howard, “Diffusion and sedimentation in colloidal suspensions using multiparticle collision dynamics with a discrete particle model,” *Journal of Chemical Physics* **156**, 024901 (2022).
- ³⁸Y. M. Wani, P. G. Kovakas, A. Nikoubashman, and M. P. Howard, “Mesoscale simulations of diffusion and sedimentation in shape-anisotropic nanoparticle suspensions,” *Soft Matter* **20**, 3942–3953 (2024).
- ³⁹M. Yetkin, Y. M. Wani, K. Kritika, M. P. Howard, M. Kappl, H.-J. Butt, and A. Nikoubashman, “Structure formation in supraparticles composed of spherical and elongated particles,” *Langmuir* **40**, 1096–1108 (2023).
- ⁴⁰J. A. Anderson, J. Glaser, and S. C. Glotzer, “Hoomd-blue: A python package for high-performance molecular dynamics and hard particle monte carlo simulations,” *Computational Materials Science* **173**, 109363 (2020).
- ⁴¹M. P. Howard, A. Statt, F. Madutsa, T. M. Truskett, and A. Z. Panagiotopoulos, “Quantized bounding volume hierarchies for neighbor search in molecular simulations on graphics processing units,” *Computational Materials Science* **164**, 139–146 (2019).
- ⁴²<https://github.com/mphowardlab/azplugins>.
- ⁴³C. Huang, A. Chatterji, G. Sutmann, G. Gompper, and R. Winkler, “Cell-level canonical sampling by velocity scaling for multiparticle collision dynamics simulations,” *Journal of Computational Physics* **229**, 168–177 (2010).
- ⁴⁴C.-C. Huang, A. Varghese, G. Gompper, and R. G. Winkler, “Thermostat for nonequilibrium multiparticle-collision-dynamics simulations,” *Physical Review E* **91**, 013310 (2015).
- ⁴⁵T. Ihle and D. M. Kroll, “Stochastic rotation dynamics: A galilean-invariant mesoscopic model for fluid flow,” *Physical Review E* **63**, 020201 (2001).
- ⁴⁶T. Ihle and D. M. Kroll, “Stochastic rotation dynamics. i. formalism, galilean invariance, and green-kubo relations,” *Physical Review E* **67**, 066705 (2003).
- ⁴⁷J. D. Weeks, D. Chandler, and H. C. Andersen, “Role of repulsive forces in determining the equilibrium structure of simple liquids,” *Journal of Chemical Physics* **54**, 5237–5247 (1971).
- ⁴⁸W. Humphrey, A. Dalke, and K. Schulten, “Vmd: Visual molecular dynamics,” *Journal of Molecular Graphics* **14**, 33–38 (1996).
- ⁴⁹A. Malevanets and J. M. Yeomans, “Dynamics of short polymer chains in solution,” *Europhysics Letters* **52**, 231–237 (2000).
- ⁵⁰Y.-S. Peng and T. Sinno, “Multiparticle collision dynamics simulations of hydrodynamic interactions in colloidal suspensions: How well does the discrete particle approach do at short range?” *Journal of Chemical Physics* **160**, 174121 (2024).
- ⁵¹G. Bussi, D. Donadio, and M. Parrinello, “Canonical sampling through velocity rescaling,” *Journal of Chemical Physics* **126**, 014101 (2007).
- ⁵²N. W. Ashcroft and D. C. Langreth, “Structure of binary liquid mixtures. i,” *Physical Review* **156**, 685–692 (1967).
- ⁵³V. Ramasubramani, B. D. Dice, E. S. Harper, M. P. Spellings, J. A. Anderson, and S. C. Glotzer, “freud: A software suite for high throughput analysis of particle simulation data,” *Computer Physics Communications* **254**, 107275 (2020).
- ⁵⁴F. Müller-Plathe, “Reversing the perturbation in nonequilibrium molecular dynamics: An easy way to calculate the shear viscosity of fluids,” *Physical Review E* **59**, 4894–4898 (1999).
- ⁵⁵C. M. Tenney and E. J. Maginn, “Limitations and recommendations for the calculation of shear viscosity using reverse nonequilibrium molecular dynamics,” *Journal of Chemical Physics* **132**, 014103 (2010).
- ⁵⁶B. Dünweg and K. Kremer, “Molecular dynamics simulation of a polymer chain in solution,” *Journal of Chemical Physics* **99**, 6983–6997 (1993).
- ⁵⁷I.-C. Yeh and G. Hummer, “System-size dependence of diffusion coefficients and viscosities from molecular dynamics simulations with periodic boundary conditions,” *Journal of Physical Chemistry B* **108**, 15873–15879 (2004).
- ⁵⁸H. Hasimoto, “On the periodic fundamental solutions of the stokes equations and their application to viscous flow past a cubic array of spheres,” *Journal of Fluid Mechanics* **5**, 317–328 (1959).
- ⁵⁹G. Mo and A. S. Sangani, “A method for computing stokes flow interactions among spherical objects and its application to suspensions of drops and porous particles,” *Physics of Fluids* **6**, 1637–1652 (1994).
- ⁶⁰J. T. Padding and A. A. Louis, “Hydrodynamic interactions and brownian forces in colloidal suspensions: Coarse-graining over

- time and length scales,” *Physical Review E* **74**, 031402 (2006).
- ⁶¹R. Verberg, I. M. de Schepper, and E. G. D. Cohen, “Viscosity of colloidal suspensions,” *Physical Review E* **55**, 3143–3158 (1997).
- ⁶²N. Kikuchi, C. M. Pooley, J. F. Ryder, and J. M. Yeomans, “Transport coefficients of a mesoscopic fluid dynamics model,” *Journal of Chemical Physics* **119**, 6388–6395 (2003).
- ⁶³E. Tüzel, M. Strauss, T. Ihle, and D. M. Kroll, “Transport coefficients for stochastic rotation dynamics in three dimensions,” *Physical Review E* **68**, 036701 (2003).
- ⁶⁴M. Ripoll, K. Mussawisade, R. Winkler, and G. Gompper, “Dynamic regimes of fluids simulated by multiparticle-collision dynamics,” *Physical Review E* **72**, 016701 (2005).
- ⁶⁵A. Statt, M. P. Howard, and A. Z. Panagiotopoulos, “Unexpected secondary flows in reverse nonequilibrium shear flow simulations,” *Physical Review Fluids* **4**, 043905 (2019).
- ⁶⁶N. F. Carnahan and K. E. Starling, “Equation of state for nonattracting rigid spheres,” *Journal of Chemical Physics* **51**, 635–636 (1969).
- ⁶⁷M. Tokuyama and I. Oppenheim, “Dynamics of hard-sphere suspensions,” *Physical Review E* **50**, R16–R19 (1994).
- ⁶⁸D. R. Foss and J. F. Brady, “Self-diffusion in sheared suspensions by dynamic simulation,” *Journal of Fluid Mechanics* **401**, 243–274 (1999).
- ⁶⁹T. G. Mason and D. A. Weitz, “Optical measurements of frequency-dependent linear viscoelastic moduli of complex fluids,” *Physical Review Letters* **74**, 1250–1253 (1995).
- ⁷⁰G. K. Batchelor, “Sedimentation in a dilute dispersion of spheres,” *Journal of Fluid Mechanics* **52**, 245–268 (1972).
- ⁷¹C.-C. Huang, G. Gompper, and R. G. Winkler, “Hydrodynamic correlations in multiparticle collision dynamics fluids,” *Physical Review E* **86**, 056711 (2012).
- ⁷²K. Qin and A. A. Zaman, “Viscosity of concentrated colloidal suspensions: comparison of bidisperse models,” *Journal of Colloid and Interface Science* **266**, 461–467 (2003).
- ⁷³H. M. Shewan and J. R. Stokes, “Analytically predicting the viscosity of hard sphere suspensions from the particle size distribution,” *Journal of Non-Newtonian Fluid Mechanics* **222**, 72–81 (2015).
- ⁷⁴C. Anzivino, M. Casiulis, T. Zhang, A. S. Moussa, S. Martiniani, and A. Zaccone, “Estimating random close packing in polydisperse and bidisperse hard spheres via an equilibrium model of crowding,” *Journal of Chemical Physics* **158**, 044901 (2023).
- ⁷⁵R. H. Davis and H. Gecol, “Hindered settling function with no empirical parameters for polydisperse suspensions,” *AIChE Journal* **40**, 570–575 (1994).
- ⁷⁶T. J. Boerner, S. Deems, T. R. Furlani, S. L. Knuth, and J. Towns, “Access: Advancing innovation: Nsf’s advanced cyberinfrastructure coordination ecosystem: Services & support,” in *Practice and Experience in Advanced Research Computing 2023: Computing for the Common Good*, PEARC ’23 (New York, NY, USA, 2023) p. 173–176.

Supplementary material for “Transport properties of monodisperse and bidisperse hard-sphere colloidal suspensions from multiparticle collision dynamics simulations”

Michael P. Howard^{a)}

*Department of Chemical Engineering, Auburn University, Auburn, AL 36849,
USA*

^{a)}Electronic mail: mphoward@auburn.edu

S1. MONODISPERSE SUSPENSIONS

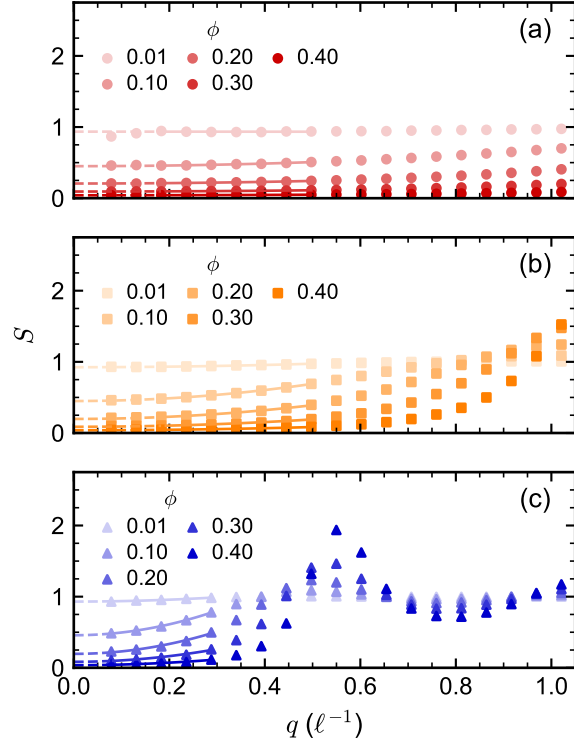


FIG. S1. Static structure factor S as a function of wavevector q for monodisperse suspensions of particles with diameter (a) 3ℓ , (b) 6ℓ , and (c) 12ℓ at selected volume fractions ϕ . The solid lines show the fit described in the main text, while the dashed lines show the extrapolation to $q = 0$.

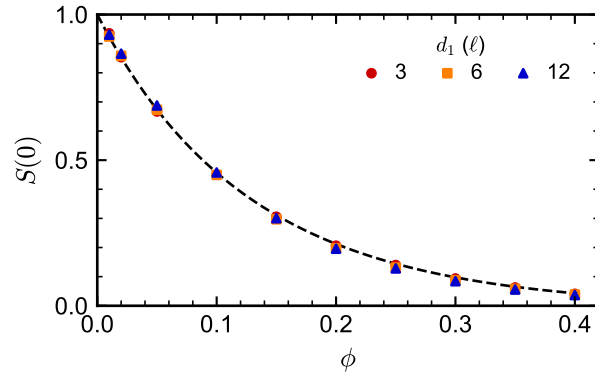


FIG. S2. Static structure factor extrapolated to $q = 0$, $S(0)$, for monodisperse suspensions of particles with diameter d_1 . The dashed line is the theoretical expectation for the Carnahan–Starling equation of state, $S(0) = (1 - \phi)^4 / (1 + 4\phi + 4\phi^2 - 4\phi^3 + \phi^4)$.

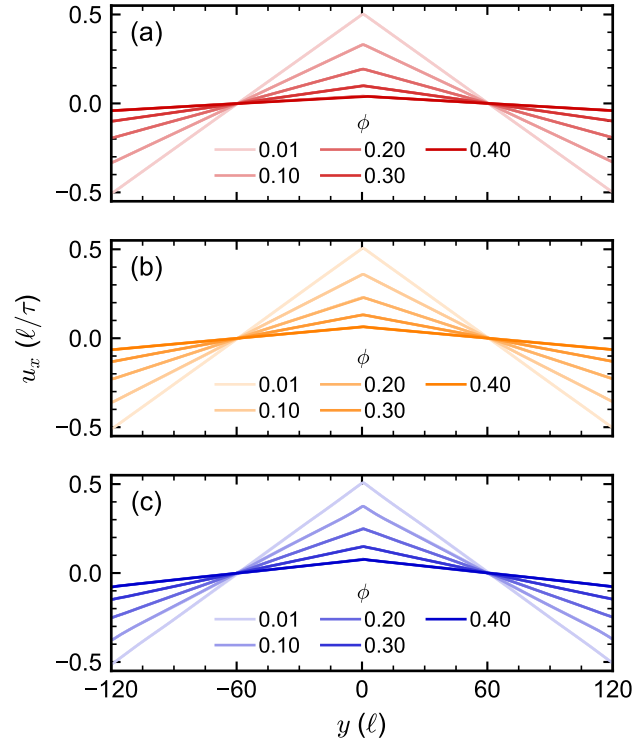


FIG. S3. Mass-averaged velocity u_x as a function of position y for monodisperse suspensions of particles with diameter (a) 3ℓ , (b) 6ℓ , and (c) 12ℓ at selected volume fractions ϕ in reverse nonequilibrium simulations.

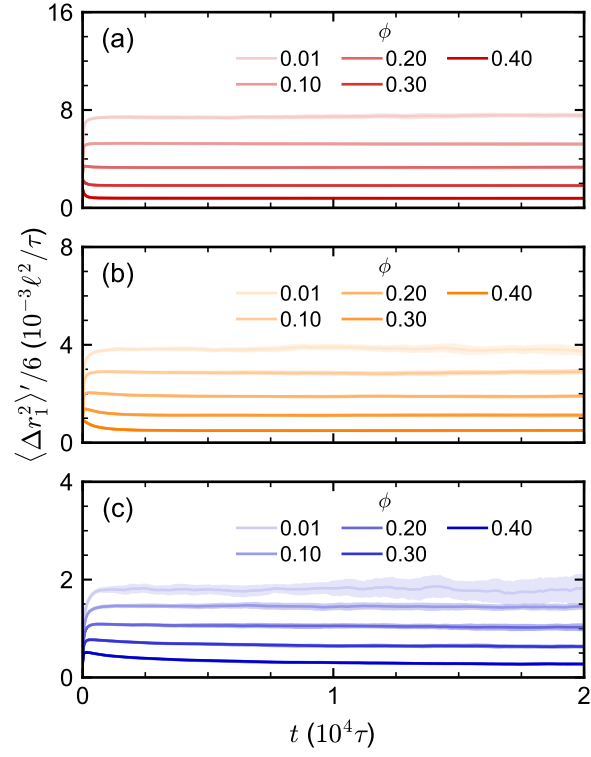


FIG. S4. Time derivative $\langle \Delta r_1^2 \rangle'$ of mean squared displacement Δr_1^2 as a function of time t for monodisperse suspensions of particles with diameter (a) 3ℓ , (b) 6ℓ , and (c) 12ℓ at selected volume fractions ϕ .

S2. BIDISPERSE SUSPENSIONS

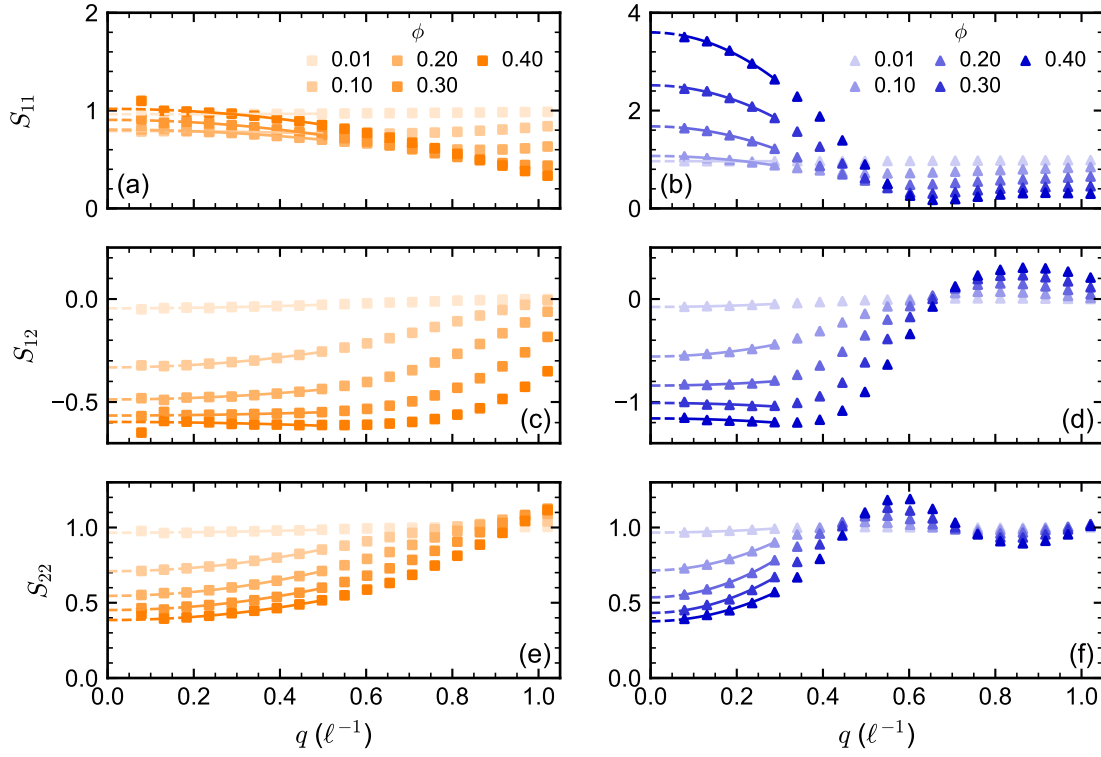


FIG. S5. Partial static structure factors (a–b) S_{11} , (c–d) S_{12} , and (e–f) S_{22} as a function of wavevector q for bidisperse suspensions of particles with diameter $d_1 = 3\ell$ and particles with diameter (a, c, e) $d_2 = 6\ell$ or (b, d, f) $d_2 = 12\ell$ at selected volume fractions ϕ . There are equal volumes of both particle types. The solid lines show the fit described in the main text, while the dashed lines show the extrapolation to $q = 0$.

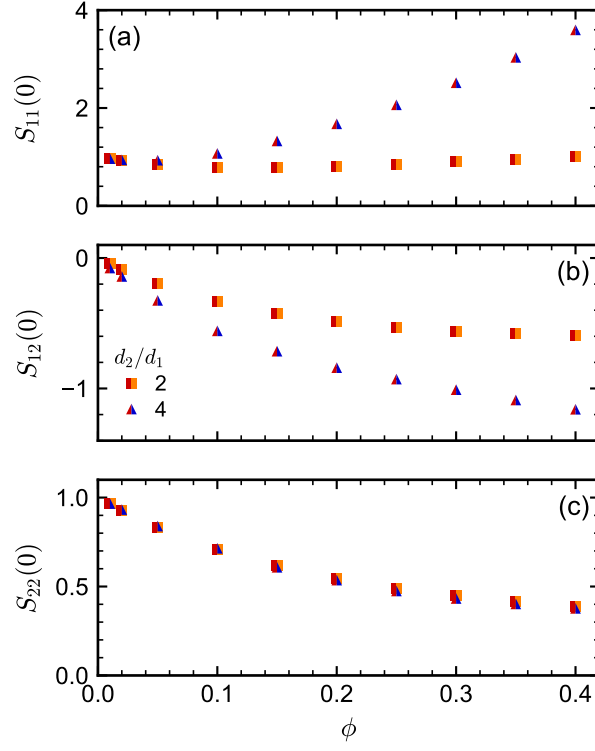


FIG. S6. Partial static structure factors extrapolated to $q = 0$, (a) $S_{11}(0)$, (b) $S_{12}(0)$, and (c) $S_{22}(0)$, for bidisperse suspensions of particles with diameters $d_1 = 3\ell$ and varied d_2 at selected volume fractions ϕ . There are equal volumes of both particle types.

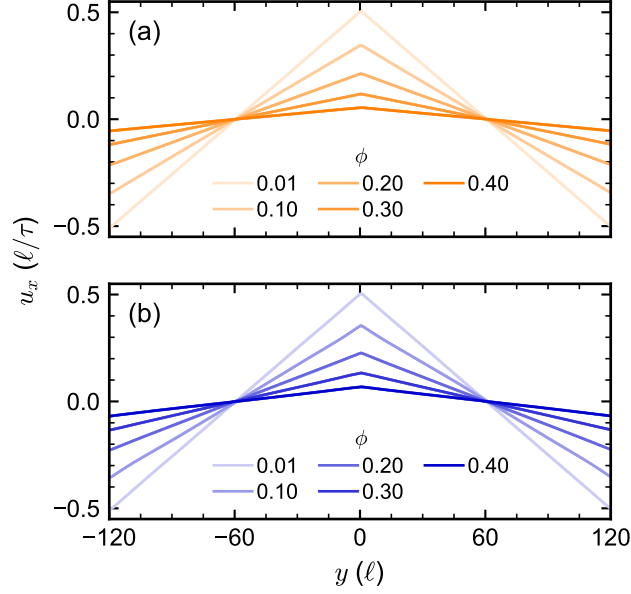


FIG. S7. Mass-averaged velocity u_x as a function of position y for bidisperse suspensions of particles with diameter $d_1 = 3 \ell$ and particles with diameter (a) $d_2 = 6 \ell$ or (b) $d_2 = 12 \ell$ at selected volume fractions ϕ in reverse nonequilibrium simulations. There are equal volumes of both particle types.

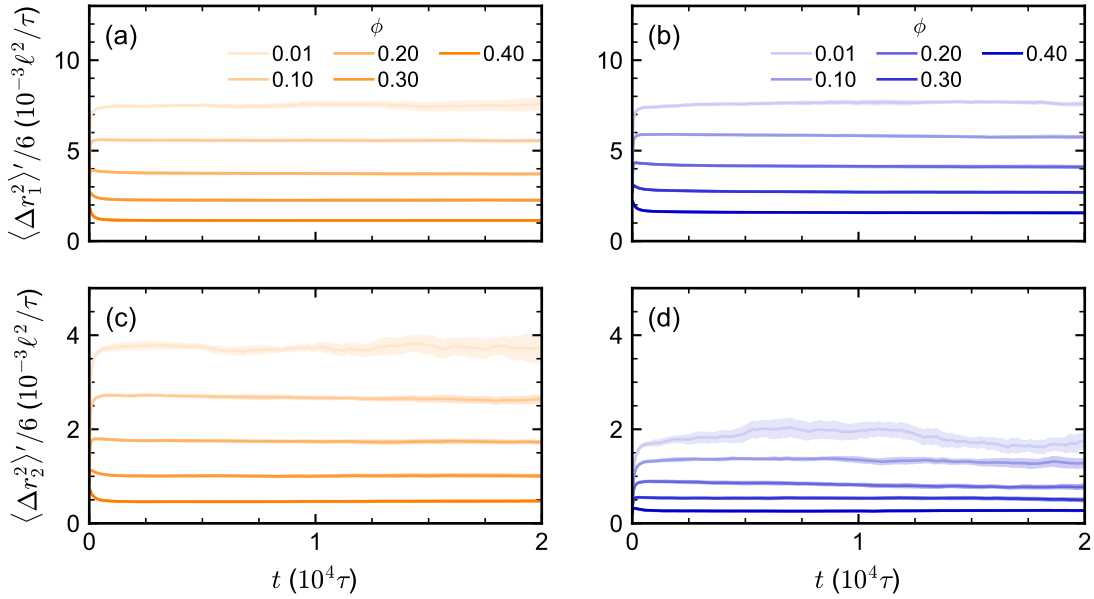


FIG. S8. Time derivative $\langle \Delta r_i^2 \rangle'$ of mean squared displacement Δr_i^2 for particles of type i as a function of time t for bidisperse suspensions of particles with diameter $d_1 = 3 \ell$ and particles with diameter (a, c) $d_2 = 6 \ell$ or (b, d) $d_2 = 12 \ell$ at selected volume fractions ϕ . There are equal volumes of both particle types.

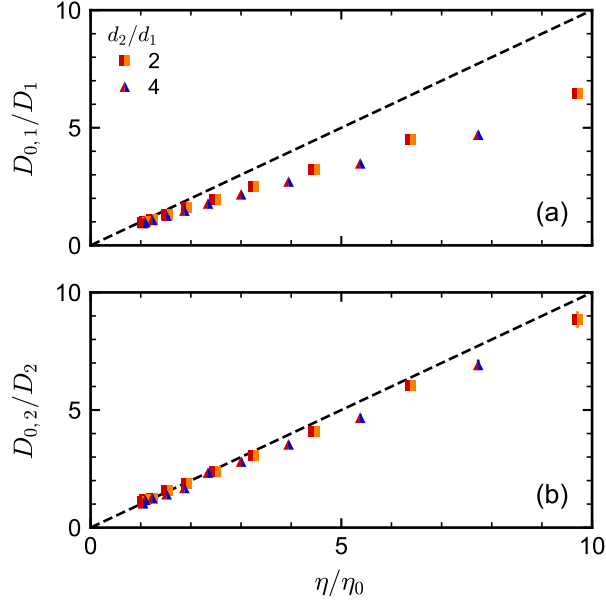


FIG. S9. Test of the generalized Stokes–Einstein relationship between the simulated shear viscosity η and long-time self-diffusion coefficients (a) D_1 and (b) D_2 for bidisperse suspensions of particles with diameter $d_1 = 3\ell$ and varied d_2 using the data from Figs. 6 and 7. The dashed line, $D_{0,i}/D_i = \eta/\eta_0$, is the theoretical expectation.

S3. SINGLE PARTICLES

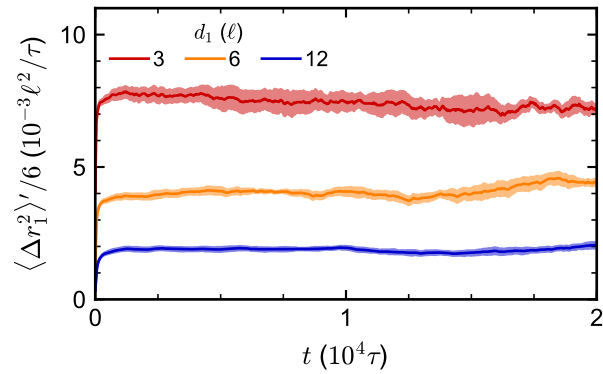


FIG. S10. Time derivative $\langle \Delta r_1^2 \rangle'$ of mean squared displacement Δr_1^2 as a function of time t for a single particle with diameter d_1 .